

# Soft x-ray absorption spectroscopy study of the electronic structures of the MnFe Prussian blue analogs $(\text{Rb}_x\text{Ba}_y)\text{Mn}_{[3-(x+2y)]/2}[\text{Fe}(\text{CN})_6]\text{H}_2\text{O}$

Eunsook Lee,<sup>1</sup> Seungho Seong,<sup>1</sup> Hyun Woo Kim,<sup>1</sup> D. H. Kim,<sup>1,\*</sup> Nidhi Thakur,<sup>2,†</sup> S. M. Yusuf,<sup>2</sup> Bongjae Kim,<sup>3</sup> B. I. Min,<sup>3</sup> Younghak Kim,<sup>4</sup> J.-Y. Kim,<sup>4</sup> F. M. F. de Groot,<sup>5</sup> and J.-S. Kang<sup>1,‡</sup>

<sup>1</sup>Department of Physics, The Catholic University of Korea, Bucheon 14662, Korea

<sup>2</sup>Solid State Physics Division, Bhabha Atomic Research Centre, Mumbai 400 085, India

<sup>3</sup>Department of Physics, Pohang University of Science and Technology, Pohang 37673, Korea

<sup>4</sup>Pohang Accelerator Laboratory (PAL), Pohang University of Science and Technology, Pohang 37673, Korea

<sup>5</sup>Department of Inorganic Chemistry and Catalysis, Utrecht University, Sorbonnelaan 16, NL-3584 Utrecht, The Netherlands

(Received 10 July 2017; revised manuscript received 24 September 2017; published 9 November 2017)

The electronic structures of Prussian blue analog  $(\text{Rb}_x\text{Ba}_y)\text{Mn}_{[3-(x+2y)]/2}[\text{Fe}(\text{CN})_6]$  cyanides have been investigated by employing soft x-ray absorption spectroscopy (XAS) and magnetic circular dichroism (XMCD) at the Fe and Mn  $L$  ( $2p$ ) edges. The measured XAS spectra have been analyzed with the configuration-interaction (CI) cluster model calculations. The valence states of the Fe and Mn ions are found to be  $\text{Fe}^{2+}$ - $\text{Fe}^{3+}$  mixed valent, with an average valency of  $\nu(\text{Fe}) \sim 2.8$  and nearly divalent ( $\text{Mn}^{2+}$ ), respectively. Our Mn/Fe  $2p$  XMCD study supports that  $\text{Mn}^{2+}$  ions are in the high-spin states while  $\text{Fe}^{2+}$ - $\text{Fe}^{3+}$  ions are in the low-spin states. The Fe and Mn  $2p$  XAS spectra are found to be essentially the same for  $80 \leq T \leq 300$  K, suggesting that a simple charge transfer upon cooling from  $\text{Fe}^{3+}$ -CN- $\text{Mn}^{2+}$  to  $\text{Fe}^{2+}$ -CN- $\text{Mn}^{3+}$  does not occur in  $(\text{Rb}_x\text{Ba}_y)\text{Mn}_{[3-(x+2y)]/2}[\text{Fe}(\text{CN})_6]$ . According to the CI cluster model analysis, it is necessary to take into account both the ligand-to-metal charge transfer and the metal-to-ligand charge transfer in describing Fe  $2p$  XAS, while the effect of charge transfer is negligible in describing Mn  $2p$  XAS. The CI cluster model analysis also shows that the trivalent  $\text{Fe}^{3+}$  ions have a strong covalent bonding with the  $\text{C} \equiv \text{N}$  ligands and are under a large crystal-field energy of  $10Dq \sim 3$  eV, in contrast to the weak covalency effect and a small  $10Dq \sim 0.6$  eV for the divalent  $\text{Mn}^{2+}$  ions.

DOI: [10.1103/PhysRevB.96.195120](https://doi.org/10.1103/PhysRevB.96.195120)

## I. INTRODUCTION

Molecule-based magnetic materials exhibit several interesting switching phenomena between two electronic states in response to a magnetic field, light, pressure, and temperature, including a photoinduced magnetization transition [1–4], a pressure-induced magnetization transition [5], and a spin crossover [6]. Among them, Prussian blue analogs (PBAs), which are represented by the general formula  $A_x M[M'(\text{CN})_6]_y \cdot m\text{H}_2\text{O}$ , where  $A$  is an alkali-metal cation and  $M$  and  $M'$  are divalent or trivalent transition-metal (TM) cations, have been studied extensively [6,7]. Both  $M$  and  $M'$  ions are located at the octahedral ( $O_h$ ) sites [8,9]. Additional alkali-metal ions can be inserted in part of the interstitial tetrahedral ( $T_d$ ) sites. CoFe and NiFe PBAs ( $M = \text{Co}, \text{Ni}$ ;  $M' = \text{Fe}$ ) crystallize in face-centered-cubic (fcc) structures, consisting of a three-dimensional (3D) coordination network containing Co-NC-Fe or Ni-NC-Fe entities [8]. Depending on  $A_x$ , MnFe PBAs ( $M = \text{Mn}$ ;  $M' = \text{Fe}$ ) exhibit diverse structural and magnetic phases. For example, some MnFe PBAs undergo structural phase transitions from an fcc ( $F\bar{4}3m$ ) structure at high temperature (HT) to a tetragonal ( $I\bar{4}m2$ ) structure at low temperature (LT) [6], with the concomitant switching phenomenon. The HT phase of  $\text{Rb}_{0.88}\text{Mn}[\text{Fe}(\text{CN})_6]_{0.96} \cdot m\text{H}_2\text{O}$  has a ferromagnetic stacking of antiferromagnetic sheets [10], while  $(\text{Rb}_x\text{Ba}_y)\text{Mn}_{[3-(x+2y)]/2}[\text{Fe}(\text{CN})_6] \cdot m\text{H}_2\text{O}$  of the

present study has an antiparallel stacking of ferromagnetic sheets along the crystallographic  $c$  direction (see Fig. 1) [11].

Understanding the physical and magnetic properties of the PBAs is very important, not only for their technical application but also for the fundamental scientific aspect. The switching phenomena, observed in a CoFe PBA [3], were often ascribed due to a charge transfer between the  $\text{Co}^{2+}(S = 3/2)$ - $\text{Fe}^{3+}(S = 1/2)$  pairs and the  $\text{Co}^{3+}(S = 0)$ - $\text{Fe}^{2+}(S = 0)$  pairs through the cyanide  $\text{C} \equiv \text{N}$  bridge. In this interpretation, the low-spin (LS)  $\text{Co}^{3+}(t_{2g}^6 e_g^0, S = 0)$  ions are transformed to the high-spin (HS)  $\text{Co}^{2+}(t_{2g}^5 e_g^2, S = 3/2)$  ions [3,12–15]. In certain  $\text{Rb}_x\text{Mn}_z[\text{Fe}(\text{CN})_6] \cdot m\text{H}_2\text{O}$  PBAs, a temperature ( $T$ )-induced phase transition with a large thermal hysteresis was observed [10,16,17]. Then, as in CoFe PBAs, the valence transition between the  $\text{Mn}^{2+}(S = 5/2)$ - $\text{Fe}^{3+}(S = 1/2)$  pairs at HT and the  $\text{Mn}^{3+}(S = 2)$ - $\text{Fe}^{2+}(S = 0)$  pairs at LT has been suggested for MnFe PBAs [6,10,16,17]. However, these models are controversial [3,9,12–17], and the experimental evidence for them is lacking. Therefore, in order to understand the origin of the switching phenomena in PBAs, it is crucial to determine the valence and spin states of  $M$  and  $M'$  ions experimentally.

X-ray absorption spectroscopy (XAS) is a powerful experimental tool for studying the valence and spin states of TM ions in solids [18,19]. Several studies on the valence states of  $M$  and  $M'$  ions in PBAs have been reported in the literature [7,8,12,17,20–22]. Some of the previous XAS studies on PBAs were done at the  $K$  edges of  $M$  and  $M'$  ions [7,8,12,17,22].  $K$ -edge ( $1s$ ) XAS for  $M$  and  $M'$  ions has the advantage of being bulk-sensitive because of the use of hard x rays. On the other hand,  $K$ -edge XAS does not reflect directly the valence

\*Present address: KRISS, Daejeon 34113, Korea.

†Present address: Department of Physics, Mithibai College, Mumbai 400056, India.

‡kangjs@catholic.ac.kr

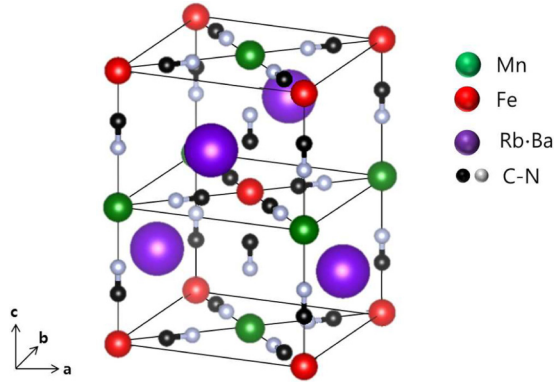


FIG. 1. Crystal structure of  $(\text{Rb}_x\text{Ba}_y)[\text{MnFe}(\text{CN})_6] \cdot m\text{H}_2\text{O}$  compounds [11].

states of  $M$  and  $M'$  ions because it is determined mainly by the  $1s \rightarrow 4p$  dipole-allowed transitions. In contrast, TM  $L$ -edge ( $2p$ ) XAS provides more direct information on the valence and spin states of TM ions because the  $2p \rightarrow 3d$  absorption process is involved. Soft x-ray magnetic circular dichroism (XMCD) is very unique in determining the spin and orbital components of the element-specific local magnetic moments of TM ions [23,24]. The  $K$ -edge XMCD [25–28] or the  $L$ -edge XMCD studies [29–31] have been reported for other kinds of PBAs. Further, there are several reports on the XAS/XMCD studies on PBA nanosystems [31–33].

In this work, we have studied the electronic structures of Ba-substituted  $(\text{Rb}_x\text{Ba}_y)\text{Mn}_z[\text{Fe}(\text{CN})_6]$  PBAs ( $z = [3 - (x + 2y)]/2$ ) (where  $m\text{H}_2\text{O}$  water molecules are omitted for clarity) by employing XAS and XMCD at the Mn and Fe  $L_3$  ( $2p_{3/2}$ ) and  $L_2$  ( $2p_{1/2}$ ) edges.  $(\text{Rb}_x\text{Ba}_y)\text{Mn}_z[\text{Fe}(\text{CN})_6]$  PBAs exhibit a switching between the antiferromagnetic phase and the ferrimagnetic-like phase under an external magnetic field [34].  $T$ -dependent variations of the  $\text{Mn}^{2+}$  and  $\text{Fe}^{3+}$  ordered magnetic moments were observed, but no structural transitions were observed in  $(\text{Rb}_x\text{Ba}_y)\text{Mn}_z[\text{Fe}(\text{CN})_6]$  PBAs [11], so that the photoinduced magnetization transition is not expected.

## II. EXPERIMENTAL DETAILS

Polycrystalline  $(\text{Rb}_x\text{Ba}_y)\text{Mn}_z[\text{Fe}(\text{CN})_6]$  ( $z = [3 - (x + 2y)]/2$ ) compounds with  $(x, y) = (0.84, 0), (0.69, 0.19), (0.19, 0.3)$  were synthesized by a co-precipitation method. Figure 1 shows the tetragonal crystal structure of  $(\text{Rb}_x\text{Ba}_y)\text{Mn}_z[\text{Fe}(\text{CN})_6]$  PBA at LT, which belongs to the  $I\bar{4}m2$  space group. Lattice constants are  $a = 7.45 \text{ \AA}$  and  $c = 10.55 \text{ \AA}$  when  $y = 0$  [11], and they decrease slightly with increasing  $\text{Ba}^{2+}$  concentration ( $y$ ). Due to the stoichiometry of these compounds, some of the Fe, C, and N sites are vacant and the O atoms of  $\text{H}_2\text{O}$  molecules occupy the empty N sites. The main feature of this structure is the presence of the 3D network of Mn-NC-Fe chains along the (110) and (001) directions. Hence, depending on the relative orientations among the  $p_\sigma$ ,  $p_\pi$ , Mn  $e_g$  and  $t_{2g}$ , and Fe  $t_{2g}$  orbitals, the ferromagnetic ordering in the  $ab$  plane and the antiferromagnetic ordering along the  $c$  axis are realized [11].

The details of the sample preparation and characterization are described in Ref. [11]. Hereafter, we will denote these

TABLE I. Labels of the  $(\text{Rb}_x\text{Ba}_y)\text{Mn}_z[\text{Fe}(\text{CN})_6] \cdot m\text{H}_2\text{O}$  PBA samples, where the nominal values of  $z = [3 - (x + 2y)]/2$  are listed. The average Fe valency  $\nu(\text{Fe})$  is explained under Fig. 5.

$(\text{Rb}_x\text{Ba}_y)\text{Mn}_z[\text{Fe}(\text{CN})_6]$	$x$	$y$	$z$	$\nu(\text{Fe})$
Rb0.84	0.84	0	1.08	2.75
Rb0.69	0.69	0.19	0.965	2.82
Rb0.19	0.19	0.3	1.105	2.75

samples as  $(\text{Rb}_x\text{Ba}_y)\text{MnFe}$  for simplicity, and we label them as Sample Rb0.84, Rb0.69, and Rb0.19 for  $(x, y) = (0.84, 0), (0.69, 0.19),$  and  $(0.19, 0.3)$ , respectively (see Table I). For these samples, the Mn content is roughly  $\sim 1$  for all three samples with small vacancies or excess. If one assumes  $\text{Mn}^{2+}$  and  $[\text{Fe}(\text{CN})_6]^{-3}$ , the nominal  $z$  values of  $z = 1.08, 0.965,$  and  $1.105$  are obtained, respectively.

XAS and XMCD experiments were performed at the 2A elliptically polarized undulator beamline of the Pohang Light Source (PLS). The chamber pressure was better than  $3 \times 10^{-10}$  Torr. Samples were mounted by using a carbon tape, and they were measured as they were. XAS and XMCD spectra were obtained by the total electron yield (TEY) via sample drain current, which has a probing depth of 50–100  $\text{\AA}$  [35]. XMCD spectra were obtained under an external magnetic field of  $H \sim 0.6T$ . The total resolution for XAS and XMCD was set at  $\sim 100$  meV at  $h\nu \sim 600$  eV. All the XAS and XMCD spectra were normalized to the incident photon flux.

## III. RESULTS AND DISCUSSION

Figure 2(a) shows the measured Fe  $2p$  ( $L$ -edge) XAS spectra of  $(\text{Rb}_x\text{Ba}_y)\text{MnFe}$  PBA samples. The Fe  $2p$  XAS spectra of  $(\text{Rb}_x\text{Ba}_y)\text{MnFe}$  PBAs are very similar to one another, indicating that the valence states of Fe ions are very

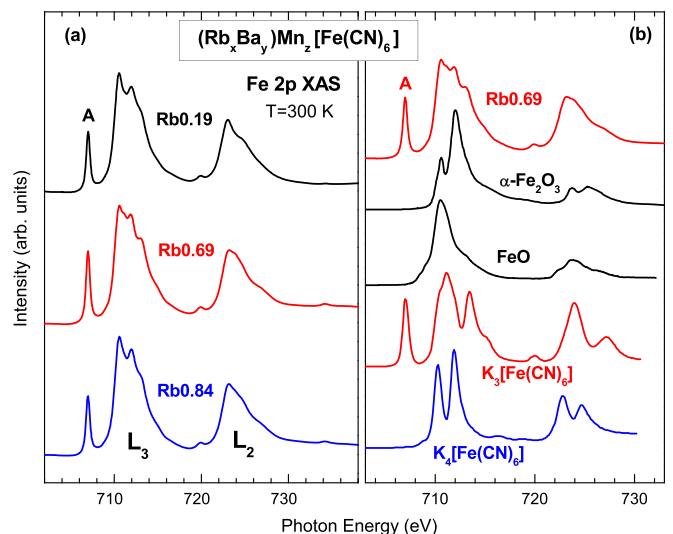


FIG. 2. (a) Fe  $2p$  XAS spectra of  $(\text{Rb}_x\text{Ba}_y)\text{MnFe}$  PBA samples. (b) Comparison of the Fe  $2p$  XAS spectrum of Rb0.69 sample [ $(x, y, z) = (0.69, 0.19, 0.965)$ ] with those of Fe reference materials, such as trivalent  $\alpha\text{-Fe}_2\text{O}_3$ , divalent FeO, trivalent  $\text{K}_3[\text{Fe}^{3+}(\text{CN})_6]$ , and divalent  $\text{K}_4[\text{Fe}^{2+}(\text{CN})_6]$ .

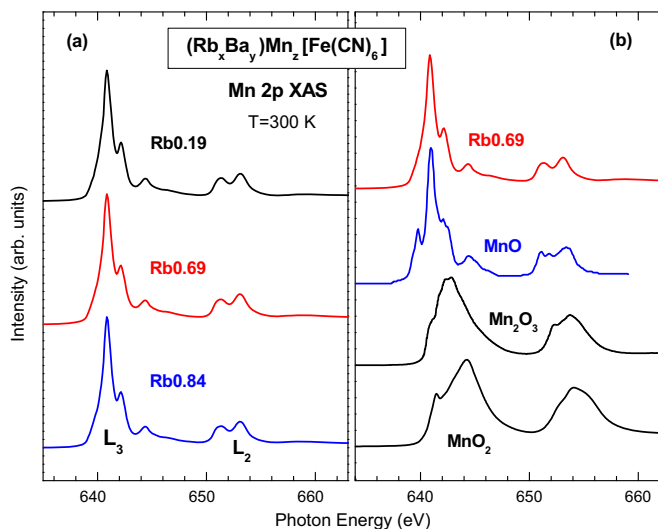


FIG. 3. (a) Mn  $2p$  XAS spectra of  $(\text{Rb}_x\text{Ba}_y)\text{MnFe}$  PBAs. (b) Comparison of Mn  $2p$  XAS spectra of the Rb0.69 sample with those of reference Mn oxides of MnS, MnO,  $\text{Mn}_2\text{O}_3$ , and  $\text{MnO}_2$ .

similar for different Ba substitutions. As a guide of the valence states of Fe ions, in Fig. 2(b) they are compared to those of divalent ( $\text{Fe}^{2+}$ ) and trivalent ( $\text{Fe}^{3+}$ ) reference materials, such as  $\alpha\text{-Fe}_2^{3+}\text{O}_3$  (Ref. [35]),  $\text{Fe}^{2+}\text{O}$  (Ref. [36]),  $\text{K}_3[\text{Fe}^{3+}(\text{CN})_6]$  (Ref. [14]), and  $\text{K}_4[\text{Fe}^{2+}(\text{CN})_6]$  (Ref. [14]).

The Fe  $2p$  XAS spectra of  $(\text{Rb}_x\text{Ba}_y)\text{MnFe}$  PBAs exhibit the features characteristic of a trivalent ( $\text{Fe}^{3+}$ ) cyanide (CN) molecule of  $\text{K}_3[\text{Fe}^{3+}(\text{CN})_6]$ , indicating that Fe ions are mainly trivalent in  $(\text{Rb}_x\text{Ba}_y)\text{MnFe}$  PBAs. In particular, the lowest-energy peak at  $\sim 707$  eV (peak A) [37] represents the trivalent  $\text{Fe}^{3+}$  state in  $(\text{Rb}_x\text{Ba}_y)\text{MnFe}$  PBAs. On the other hand, the Fe  $2p$  XAS spectra of  $(\text{Rb}_x\text{Ba}_y)\text{MnFe}$  PBAs are quite different from those of Fe oxides of  $\alpha\text{-Fe}_2\text{O}_3$  and  $\text{FeO}$ . This finding implies that Fe ions in  $(\text{Rb}_x\text{Ba}_y)\text{MnFe}$  PBAs have a strong covalent bonding with  $(\text{C} \equiv \text{N})^{-1}$  ligands, but a very weak bonding with  $\text{O}(\text{H}_2\text{O})$ . That is, the character of bonding of Fe ions with near neighbors in these  $(\text{Rb}_x\text{Ba}_y)\text{MnFe}$  PBAs is determined mainly by that with  $(\text{CN})^{-}$  ligands similarly as in  $\text{K}_n[\text{Fe}(\text{CN})_6]$  cyanide molecules.

A close look at Fig. 2(b) reveals that the line shapes of the Fe  $2p$  XAS spectra of  $(\text{Rb}_x\text{Ba}_y)\text{MnFe}$  PBAs are slightly different from that of  $\text{K}_3[\text{Fe}^{3+}(\text{CN})_6]$  and that they indeed have some characteristic features of  $\text{K}_4[\text{Fe}^{2+}(\text{CN})_6]$ . Such differences indicate that the valence states of Fe ions in  $(\text{Rb}_x\text{Ba}_y)\text{MnFe}$  PBAs are slightly  $\text{Fe}^{2+}$ - $\text{Fe}^{3+}$  mixed-valent. This conclusion is supported by the cluster model analysis (see Fig. 5).

Figure 3(a) shows the measured Mn  $2p$  XAS spectra of  $(\text{Rb}_x\text{Ba}_y)\text{MnFe}$  PBA samples. As a guide for the valence states of Mn ions, they are compared to those of divalent ( $\text{Mn}^{2+}$ ), trivalent ( $\text{Mn}^{3+}$ ), and tetravalent ( $\text{Mn}^{4+}$ ) reference oxides in Fig. 3(b), such as  $\text{Mn}^{2+}\text{O}$  (Ref. [38]),  $\text{Mn}_2^{3+}\text{O}_3$  (Ref. [39]), and  $\text{MnO}_2$  (Refs. [38,39]). Similarly as in Fe  $2p$  XAS, the Mn  $2p$  XAS spectra of  $(\text{Rb}_x\text{Ba}_y)\text{MnFe}$  PBAs are almost the same, suggesting that the valence states of Mn ions do not change for different Ba substitutions. Further, the Mn  $2p$  XAS spectra of

$(\text{Rb}_x\text{Ba}_y)\text{MnFe}$  PBAs are very similar to that of divalent  $\text{MnO}$ , suggesting that Mn ions are nearly divalent in  $(\text{Rb}_x\text{Ba}_y)\text{MnFe}$  PBAs. Differently from the Fe case, the Mn  $2p$  XAS spectra of  $(\text{Rb}_x\text{Ba}_y)\text{MnFe}$  PBAs are very similar to that of solid  $\text{MnO}$  oxide, which has no  $(\text{CN})^{-}$  ligands, suggesting that Mn ions in  $(\text{Rb}_x\text{Ba}_y)\text{MnFe}$  have a weaker bonding to  $(\text{CN})^{-}$  ligands, in contrast to Fe ions. This conclusion is supported by the cluster model analysis (see Fig. 6). According to the crystal structure (see Fig. 1), Mn ions bond to the N side of the CN ligand, while Fe ions bond to the C side of the CN ligand, which may be the reason for the different bonding character of Fe and Mn ions in  $(\text{Rb}_x\text{Ba}_y)\text{MnFe}$  PBAs.

To understand the electronic structures of  $(\text{Rb}_x\text{Ba}_y)\text{MnFe}$  PBAs microscopically, we have analyzed the Fe and Mn  $2p$  XAS spectra by employing the configuration-interaction (CI) cluster model calculations, where both the ligand-to-metal charge transfer (LMCT), i.e., the ligand-donor bonding, and the metal-to-ligand charge transfer (MLCT), i.e., the ligand-acceptor bonding, were included. LMCT and MLCT occur due to the  $\pi/\sigma$  donation and the  $\pi$  back-donation, respectively. A very pedagogical analysis for the Fe  $2p$  XAS spectra of  $\text{K}_3[\text{Fe}^{3+}(\text{CN})_6]$  and  $\text{K}_4[\text{Fe}^{2+}(\text{CN})_6]$  cyanide molecules [20] and a similar analysis for Li-inserted  $\text{Li}_x\text{Mn}[\text{Fe}(\text{CN})_6]$  PBA [21] have been reported. In the combined LMCT-MLCT charge-transfer multiplet (CTM) calculations, the free atomic multiplets due to the six CN ligand-ion environment are calculated by including the crystal-field energy  $10Dq$ , hybridization hopping parameters of  $V_{eg}$  and  $V_{t2g}$ , the repulsive  $3d$ - $3d$  Coulomb interaction  $U_{dd}$ , and the attractive  $2p$ - $3d$  Coulomb interaction  $U_{pd}$ . The energy levels of  $3d$  orbitals are split by  $10Dq$ , corresponding to the energy separation between  $t_{2g}$  and  $e_g$  orbitals. The hybridization hopping parameters of  $V_{eg}$  and  $V_{t2g}$  take account of the covalency between TM  $3d$  and ligand  $p$  states [18]. Namely,  $V_{eg}$  ( $V_{t2g}$ ) corresponds to the hopping energy between Fe  $e_g$  ( $t_{2g}$ ) and CN  $\sigma/\pi$  orbitals.

In these CI calculations,  $U_{dd} = 2.0$  eV and  $U_{pd} = 1.0$  eV were used for both  $\text{Fe}^{3+}$  and  $\text{Fe}^{2+}$  states. The charge-transfer (CT) parameters, employed in these calculations, are  $EG2$ ,  $EG3$ ,  $EF2$ , and  $EF3$ , where  $EG2 \equiv E(d^{n-1}L^-) - E(d^n)$  and  $EG3 \equiv E(d^{n-1}L^-) - E(d^{n+1}\underline{L})$  for ground-state MLCT and LMCT, respectively, and  $EF2 \equiv E(\underline{c}d^{n-1}L^-) - E(\underline{c}d^n)$

TABLE II. Electronic structure parameters used in the LMCT-MLCT combined CTM calculations. The relationship between the final-state and ground-state energies is given by  $EF = EG + U_{dd} - U_{pd}$  ( $U_{dd}$ :  $3d$  on-site Coulomb energy,  $U_{pd}$ : core-hole potential) [20].  $EG2 \equiv d^{n-1}L^- - d^n$ ;  $EG3 \equiv d^{n-1}L^- - d^{n+1}\underline{L}$ ;  $EF2 \equiv \underline{c}d^{n-1}L^- - \underline{c}d^n$ ;  $EF3 \equiv \underline{c}d^{n-1}L^- - \underline{c}d^{n+1}\underline{L}$ , where  $\underline{c}$ ,  $L^-$ , and  $\underline{L}$  denote a core hole, an extra CN ligand electron, and a CN ligand hole, respectively.  $V_{eg}$  ( $V_{t2g}$ ): the hopping energy for the  $e_g$  ( $t_{2g}$ ) symmetry.

	LMCT					LMCT			
	$10Dq$ (eV)	EG2 (eV)	EF2 (eV)	$V_{eg}$ (eV)	$V_{t2g}$ (eV)	EG3 (eV)	EF3 (eV)	$V_{eg}$ (eV)	$V_{t2g}$ (eV)
$\text{Fe}^{3+}$ ( $n = 5$ )	3.0	1.0	0.5	0.9	2.0	1.0	1.5	2.1	0.6
$\text{Fe}^{2+}$ ( $n = 6$ )	3.7	2.1	1.6	1.4	1.65	-2.0	0.0	1.4	0.6

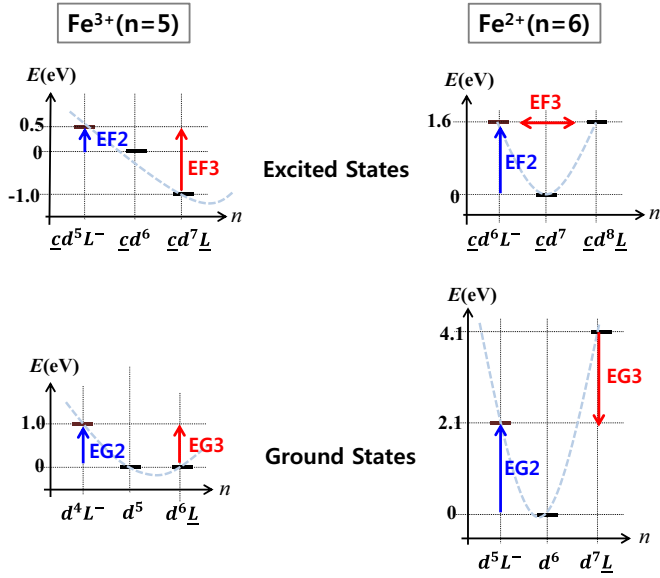


FIG. 4. (a) The relative energy levels of the ground and final states for  $\text{Fe}^{3+}$  and  $\text{Fe}^{2+}$  valence states, obtained from the combined LMCT-MLCT calculations, as shown in Table II.

and  $EF3 \equiv E(\underline{c}d^{n-1}L^-) - E(\underline{c}d^{n+1}\underline{L})$  for final-state MLCT and LMCT, respectively. Here  $\underline{c}$ ,  $L^-$ , and  $\underline{L}$  denote a Fe  $2p$  core hole, an extra CN ligand electron, and a CN ligand hole, respectively.

Table II shows the parameter values used in the LMCT-MLCT CTM calculations, and Fig. 4 shows the relative energy

levels, corresponding to those parameters in Table II. The calculated Fe  $2p$  XAS spectra for  $\text{Fe}^{2+}$ ,  $\text{Fe}^{3+}$ , and the weighted sum of  $\text{Fe}^{2+}$  and  $\text{Fe}^{3+}$  are shown in Figs. 5(a)–5(c), and a comparison between the weighted sum and the measured Fe  $2p$  XAS for the Rb0.69 sample is shown in Fig. 5(d). Here, the calculated multiplets are broadened with both the Gaussian and Lorentzian functions. The Lorentzian broadening,  $2\gamma$ , describes the core-hole lifetime [40], while the Gaussian broadening (GB) simulates the instrumental resolution. In the calculated spectra, the value of GB = 0.1 eV was fixed (see Sec. II). Figure 5(d) shows that the weighted sum of  $\text{Fe}^{2+}$  and  $\text{Fe}^{3+}$ , with the area under  $\text{Fe}^{2+}$  and  $\text{Fe}^{3+}$  being 0.18 : 0.82, yields a good fitting to the measured Fe  $2p$  XAS spectrum of the Rb0.69 PBA, corresponding to the average Fe valency of  $\nu(\text{Fe}) = 2.82$ . The  $\nu(\text{Fe})$  values for all  $(\text{Rb}_x\text{Ba}_y)\text{MnFe}$  PBA samples, obtained from the CI analysis, are listed in Table I.

The major findings of the CI cluster model calculations for Fe  $2p$  XAS are as follows. First, the sharp, low-energy peak (A) corresponds to the trivalent  $\text{Fe}^{3+}$  states and arises from the large crystal-field energy ( $10Dq \sim 3$  eV). Secondly, it is necessary to take into account both the LMCT and the MLCT in order to describe the measured Fe  $2p$  XAS spectra of  $(\text{Rb}_x\text{Ba}_y)\text{MnFe}$  PBAs. Thirdly, Fe ions are found to be in the  $\text{Fe}^{2+}$ - $\text{Fe}^{3+}$  mixed-valent states rather than in the purely integer-valence states, with the average valence states of  $\nu(\text{Fe}) \sim 2.8$  in  $(\text{Rb}_x\text{Ba}_y)\text{MnFe}$  PBAs. This finding supports the previous finding of Fig. 2.

According to the energy level diagram (see Fig. 4),  $d^5$  and  $d^6\underline{L}$  configurations contribute almost equally to the  $\text{Fe}^{3+}$

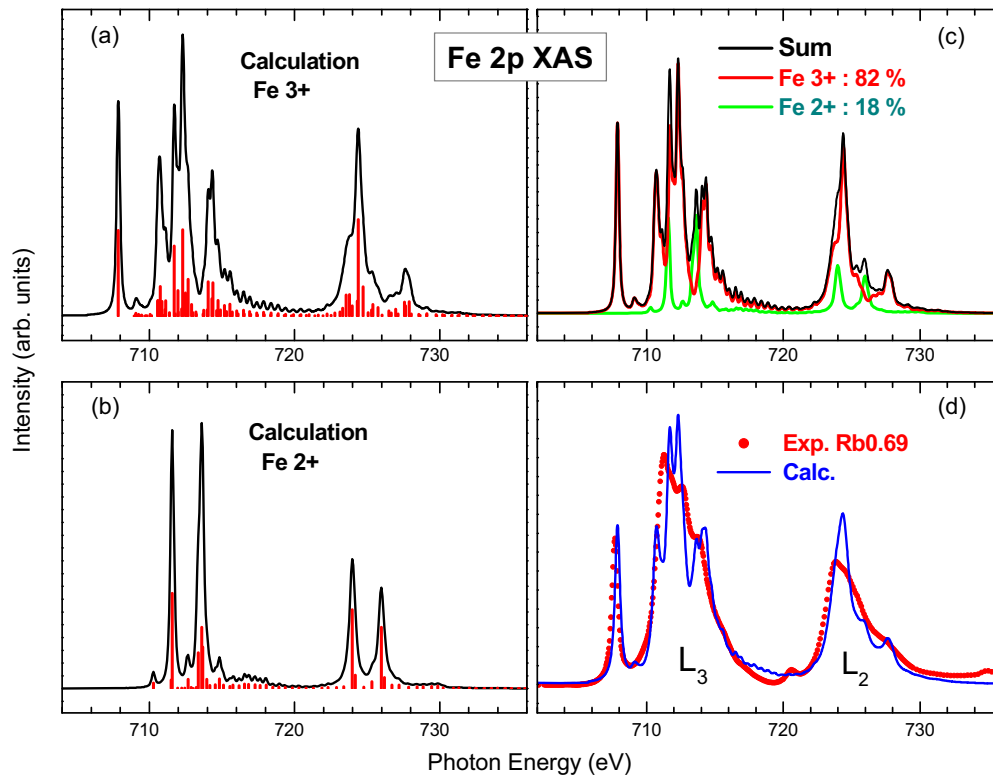


FIG. 5. The calculated  $2p$  XAS spectra for (a)  $\text{Fe}^{3+}$ , (b)  $\text{Fe}^{2+}$ , and (c) the weighted sum of  $\text{Fe}^{2+}$  and  $\text{Fe}^{3+}$ , with the area ratio of  $\text{Fe}^{2+} : \text{Fe}^{3+} = 0.18 : 0.82$ , with GB = 0.1 eV and  $2\gamma = 0.1/0.2$  eV for  $L_3/L_2$ . (d) The comparison between the weighted sum of the calculations and the measured Fe  $2p$  XAS spectrum for the Rb0.69 PBA, where GB = 0.1 eV and  $2\gamma = 0.2/0.4$  eV for  $L_3/L_2$  are employed for the calculated XAS.

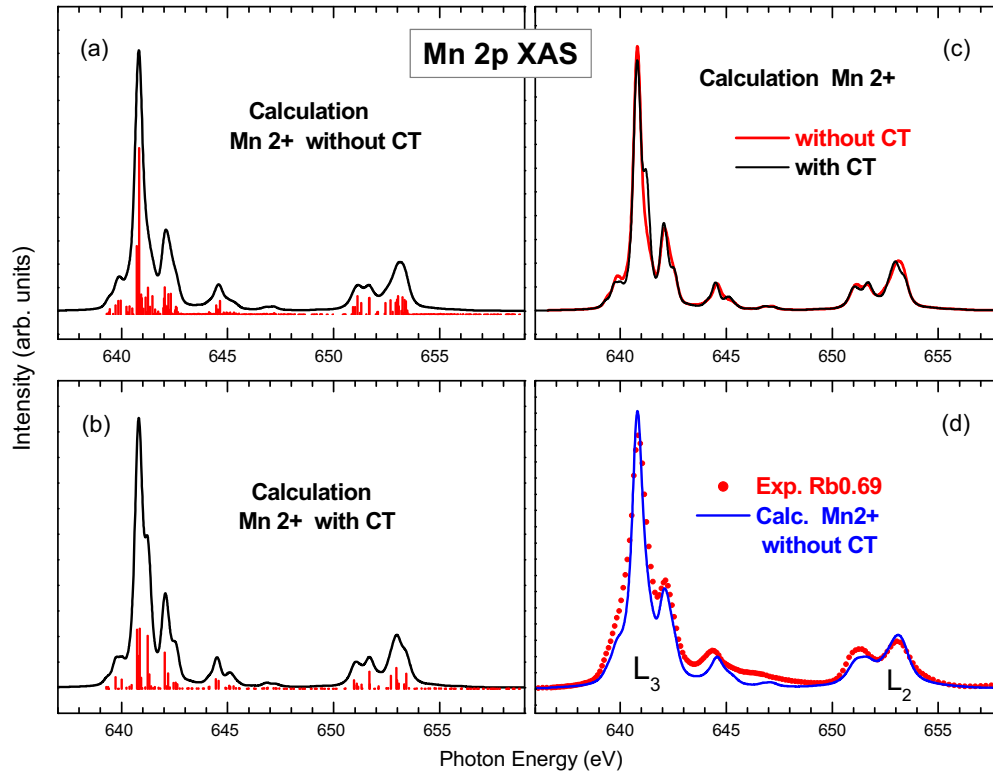


FIG. 6. The calculated  $\text{Mn}^{2+}$   $2p$  XAS spectra, obtained (a) without including CT, (b) including CT, and (c) a comparison between (a) and (b), with  $\text{GB} = 0.1$  eV and  $2\gamma = 0.1/0.2$  eV for  $L_3/L_2$ . (d) A comparison of the calculated  $\text{Mn}^{2+}$  XAS without CT with the measured  $\text{Mn} 2p$  XAS for the Rb0.69 PBA, where  $\text{GB} = 0.1$  eV and  $2\gamma = 0.2/0.4$  eV for  $L_3/L_2$  are employed for the calculated XAS.

ground states, and the  $\underline{c}d^7\underline{L}$  configuration is the lowest in the  $\text{Fe}^{3+}$  excited (final) states. Hence Fig. 4 shows that the trivalent  $\text{Fe}^{3+}$  ions have a strongly covalent bonding with  $(\text{C} \equiv \text{N})^{-1}$  ligands and that the effects of LMCT and MLCT are important in the  $\text{Fe}^{3+}$  states. In contrast, the  $\text{Fe}^{2+}$  ground and excited (final) states consist of nearly pure  $d^6$  and  $\underline{c}d^7$  configurations, respectively, indicating that the effects of LMCT and MLCT are negligible for the  $\text{Fe}^{2+}$  states.

Figure 6 shows the calculated  $\text{Mn} 2p$  XAS spectra: (a) and (b) show the  $\text{Mn} 2p$  XAS for  $\text{Mn}^{2+}$ , calculated without and with including CT, respectively, (c) shows a comparison between (a) and (b), and (d) shows a comparison between the calculated  $\text{Mn}^{2+}$  XAS without CT and the measured  $\text{Mn} 2p$  XAS for the Rb0.69 PBA. For these calculations,  $10Dq = 0.6$  eV was employed. For the calculation including CT,  $U_{dd} = 5.2$  eV,  $U_{pd} = 6.2$  eV, and  $\Delta = 6.5$  eV were employed, where  $\Delta$  is the energy needed to transfer one electron from the CN ligand band to the  $\text{Mn} 3d$  orbital. Similarly as in  $\text{Fe} 2p$  calculations (Fig. 5),  $\text{GB} = 0.1$  eV was fixed for all the calculated spectra to simulate the instrumental resolution (see Sec. II). The same  $2\gamma$  values as for the  $\text{Fe} 2p$  XAS calculations were used for the  $\text{Mn} 2p$  XAS calculations [40].

According to Fig. 6, the calculated  $\text{Mn}^{2+}$  spectrum with  $10Dq = 0.6$  eV describes the measured  $\text{Mn} 2p$  XAS spectra of  $(\text{Rb}_x\text{Ba}_y)\text{MnFe}$  PBA very well. Further, the calculated  $\text{Mn}^{2+}$  spectrum, obtained by including CT, is very similar to that obtained without including CT, indicating that the effect of CT is negligible for the  $\text{Mn}^{2+}$  ions in  $(\text{Rb}_x\text{Ba}_y)\text{MnFe}$  PBA.

This makes a sharp contrast to the  $\text{Fe}^{3+}$  ions in  $(\text{Rb}_x\text{Ba}_y)\text{MnFe}$  PBA.

As shown in Fig. 7, finite  $\text{Mn} 2p$  XMCD signals are observed in  $(\text{Rb}_x\text{Ba}_y)\text{MnFe}$  PBAs even though they are very weak, whereas the measured  $\text{Fe} 2p$  XMCD signals are almost zero (not shown in this paper). In Fig. 7(a),  $\text{Mn} 2p$  XMCD spectra of three different  $(\text{Rb}_x\text{Ba}_y)\text{MnFe}$  PBAs are compared, which indicates that the XMCD line shapes are very similar to one another. In Fig. 7(b), the  $\text{Mn} 2p$  XAS and XMCD spectra of the Rb0.69 PBA are shown as a typical example. Then, Fig. 7(c) compares the  $\text{Mn} 2p$  XMCD spectrum of Rb0.69 with that of a divalent ( $\text{Mn}^{2+}$ ) ferrimagnetic  $\text{Mn}$  oxide  $\text{MnFe}_2\text{O}_4$  as a reference [41]. The intensities of the  $\text{Mn} 2p$  XMCD signals, with respect to the  $\text{Mn} 2p$  XAS signals,  $I(\Delta\rho)/I(\text{XAS})$ , are plotted in Fig. 7(d), which shows that  $I(\Delta\rho)/I(\text{XAS})$  does not change much for different Ba concentrations.

Note that the very weak ( $\sim 0.4\%$ ) but finite  $\text{Mn} 2p$  XMCD signals are observed in all of  $(\text{Rb}_x\text{Ba}_y)\text{MnFe}$  PBAs above the Néel temperature ( $T_N \sim 10.6\text{--}13.5$  K) [11] [see Fig. 7(d)]. We think that this is because the magnetic moments of  $\text{Mn}$  ions are locally aligned due to the applied magnetic field during XMCD measurements. In addition, the XMCD line shapes are very similar to that of ferrimagnetic spinel oxide of divalent  $\text{MnFe}_2\text{O}_4$ , where  $\text{Mn}$  ions are in the HS states [41]. Hence the measured  $\text{Mn} 2p$  XMCD spectra for  $(\text{Rb}_x\text{Ba}_y)\text{MnFe}$  PBAs confirm the HS  $\text{Mn}^{2+}$  states ( $t_{2g}^3 e_g^2$ ,  $S = 5/2$ ). On the other hand, the negligibly weak  $\text{Fe} 2p$  XMCD signals in  $(\text{Rb}_x\text{Ba}_y)\text{MnFe}$  PBAs (not shown in this paper) suggest that  $\text{Fe}$  ions are in the LS states of  $\text{Fe}^{3+}$  ( $t_{2g}^5 e_g^0$ ,  $S = 1/2$ ) and

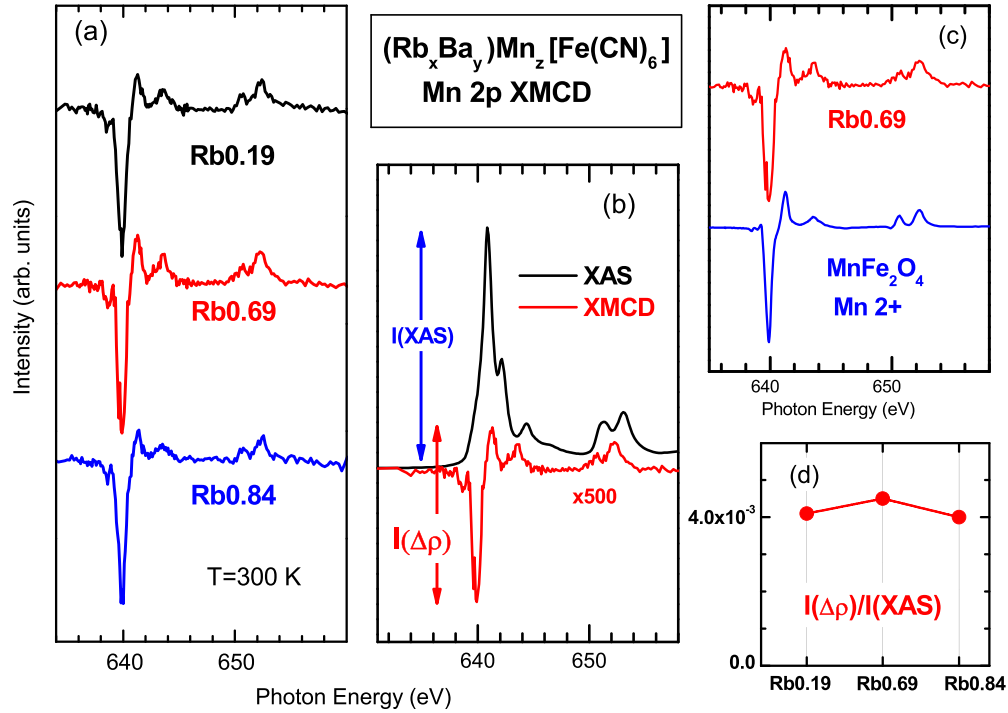


FIG. 7. (a) Mn 2p XMCD spectra of  $(\text{Rb}_x\text{Ba}_y)\text{MnFe}$  PBAs. (b) Typical Mn 2p XAS and XMCD spectra of a  $\text{Rb}_x\text{Ba}_y\text{MnFe}$  (Rb0.69) PBA. (c) Comparison of the Mn 2p XMCD spectrum of the Rb0.69 PBA with that of a divalent reference oxide of  $\text{MnFe}_2\text{O}_4$  ( $\text{Mn}^{2+}$ ). (d) Intensity plots of Mn 2p XMCD signals with respect to those of XAS,  $I(\Delta\rho)/I(\text{XAS})$ , for  $(\text{Rb}_x\text{Ba}_y)\text{MnFe}$  PBAs.  $I(\Delta\rho)$  and  $I(\text{XAS})$  are denoted in (b).

$\text{Fe}^{2+}$  ( $t_{2g}^6 e_g^0$ ,  $S = 0$ ), respectively. To determine the spin and orbital magnetic moments of Mn ions, we have analyzed the Mn 2p XMCD spectra using the XMCD sum rule [23,24,42]. The results from the sum-rule analysis are summarized in Table III. They show that the orbital magnetic moments  $m_{\text{orb}}$  of Mn ions are negligibly small in  $(\text{Rb}_x\text{Ba}_y)\text{MnFe}$  PBAs ( $m_{\text{orb}}/m_{\text{spin}} < 3\%$ ).

We now discuss the  $T$ -dependent electronic structures of  $(\text{Rb}_x\text{Ba}_y)\text{MnFe}$  PBAs. Figure 8 shows the  $T$ -dependent Fe 2p and Mn 2p XAS spectra of  $(\text{Rb}_x\text{Ba}_y)\text{MnFe}$  PBA for Rb0.69 in the temperature range of  $80 \leq T \leq 300$  K. Due to the charging problem in these PBA samples [43], the spectra obtained at low  $T$  are not good. For example, those at  $T = 150$  K are very noisy, and the Fe 2p XAS line shape at 80 K is bad. Even though some data are noisy, Fig. 8 shows clearly that the line shapes of both the Fe 2p and Mn 2p XAS spectra are essentially the same between  $80 \leq T \leq 300$  K, reflecting that the  $\text{Fe}^{2+}\text{-Fe}^{3+}$  mixed-valent states and  $\text{Mn}^{2+}$  states do

not change for  $T \geq \sim 80$  K. Thus the  $T$ -dependent XAS study provides evidence that our  $(\text{Rb}_x\text{Ba}_y)\text{MnFe}$  PBA samples do not undergo charge transfer upon cooling. It is noteworthy that, according to Fe  $K$  edge XAS at  $T = 300$  K, the Fe ions in switchable  $\text{RbMnFe}(\text{CN})_6$  are also  $\text{Fe}^{2+}\text{-Fe}^{3+}$  mixed-valent [17]. This feature suggests that a simple integer charge transfer upon cooling from  $\text{Fe}^{3+}\text{-CN-Mn}^{2+}$  to  $\text{Fe}^{2+}\text{-CN-Mn}^{3+}$  might not occur even in switchable MnFe PBAs, as proposed earlier [6,16,17]. A further XAS/XMCD study at very low temperature would be highly desirable to resolve the issue for the origin of the photoinduced transition in PBAs. As explained in Ref. [43], it is very challenging to overcome the severe charging problem in the XAS/XMCD study of PBA samples.

#### IV. CONCLUSIONS

The electronic structures of  $(\text{Rb}_x\text{Ba}_y)\text{MnFe}$  PBAs have been investigated by employing synchrotron-radiation-excited XAS and XMCD, and the measured XAS spectra have been analyzed with the CI cluster model calculations. We have found that Fe ions are  $\text{Fe}^{2+}\text{-Fe}^{3+}$  mixed-valent, with the Fe average valency of  $\nu(\text{Fe}) \sim 2.8$ , and in LS configurations, while Mn ions are nearly divalent and in HS states. According to the CI cluster model analysis, it is necessary to take into account both the LMCT and the MLCT in describing Fe 2p XAS, while the effect of CT is negligible in describing Mn 2p XAS. The trivalent  $\text{Fe}^{3+}$  ions are found to have a strong covalent bonding

TABLE III. The spin and orbital magnetic moments of the divalent  $\text{Mn}^{2+}$  ions in  $(\text{Rb}_x\text{Ba}_y)\text{Mn}_z[\text{Fe}(\text{CN})_6]$  PBAs (given in units of  $\mu_B/\text{atom}$ ).

	$m_{\text{spin}}$	$m_{\text{orb}}$	$m_{\text{orb}}/m_{\text{spin}}$
Rb0.84	$8.6 \times 10^{-3}$	$1.86 \times 10^{-4}$	0.022
Rb0.69	$6.5 \times 10^{-3}$	$1.48 \times 10^{-4}$	0.023
Rb0.19	$8.4 \times 10^{-3}$	$1.64 \times 10^{-4}$	0.020

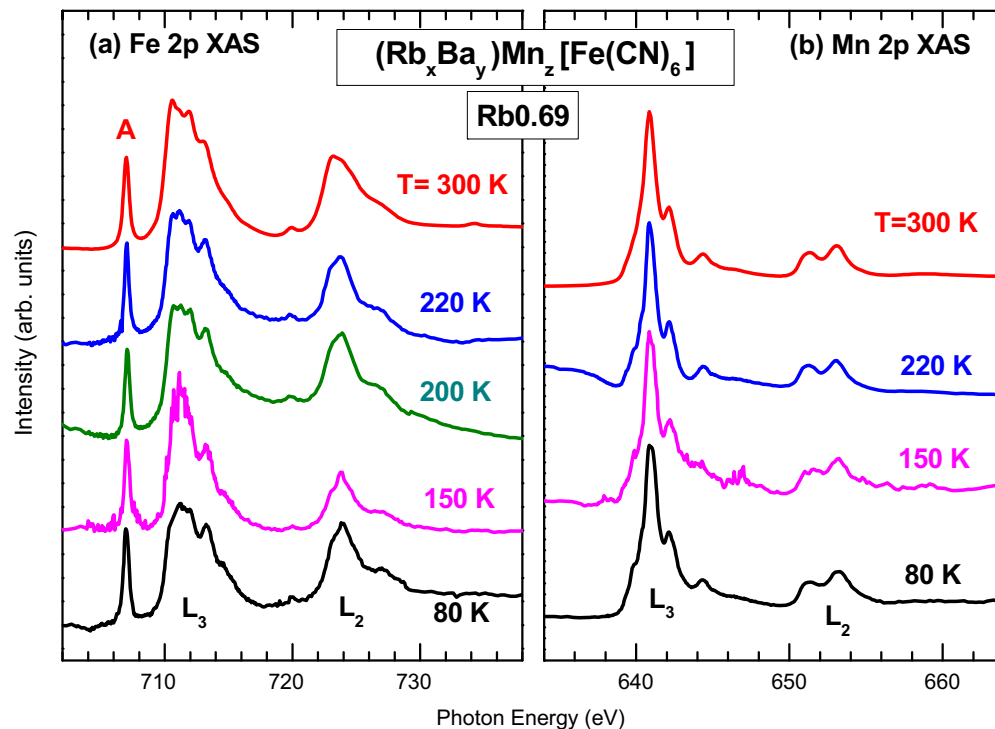


FIG. 8. Temperature ( $T$ )-dependent XAS spectra of  $(\text{Rb}_x\text{Ba}_y)\text{Mn}_z[\text{Fe}(\text{CN})_6]$  (Rb0.69) for  $80 \leq T \leq 300$  K. (a)  $T$ -dependent Fe  $2p$  XAS spectra. (b)  $T$ -dependent Mn  $2p$  XAS spectra.

with the  $\text{C} \equiv \text{N}$  ligands and to be under a large crystal-field energy of  $10Dq \sim 3$  eV. In contrast, the divalent  $\text{Mn}^{2+}$  ions are found to have a weak covalency effect and to be under a small  $10Dq \sim 0.6$  eV. The measured Mn and Fe  $2p$  XMCD spectra for  $(\text{Rb}_x\text{Ba}_y)\text{MnFe}$  support the HS  $\text{Mn}^{2+}$  states ( $t_{2g}^3e_g^2$ ;  $S = 5/2$ ) and the LS  $\text{Fe}^{2+}$  ( $t_{2g}^6e_g^0$ ;  $S = 0$ )- $\text{Fe}^{3+}$  ( $t_{2g}^5e_g^0$ ;  $S = 1/2$ ) states, respectively. The  $T$ -dependent Fe  $2p$  and Mn  $2p$  XAS spectra are essentially the same for  $80 \leq T \leq 300$  K. These findings suggest that a simple integer-valence transition model

proposed for the photoinduced magnetization transitions in MnFe PBAs needs to be reexamined more carefully.

#### ACKNOWLEDGMENTS

This work was supported by the National Research Foundation of Korea (NRF) under Contracts No. 2016R1D1A1B03932391 and No. 2017R1A2B4005175. Synchrotron experiments at PLS were supported by MSIP and PAL.

- [1] J. M. Manriquez, G. T. Yee, R. S. Mclean, A. J. Epstein, and J. S. Miller, *Science* **252**, 1415 (1991).
- [2] S. Ferlay, T. Mallah, R. Ouahes, P. Veillet, and M. Verdagner, *Nature (London)* **378**, 701 (1995).
- [3] O. Sato, T. Iyoda, A. Fujishima, and K. Hashimoto, *Science* **272**, 704 (1996).
- [4] S.-i. Ohkoshi, T. Iyoda, A. Fujishima, and K. Hashimoto, *Phys. Rev. B* **56**, 11642 (1997).
- [5] E. Coronado, M. C. Giménez-López, G. Levchenko, F. M. Romero, V. García-Baonza, A. Milner, and M. Paz-Pasternak, *J. Am. Chem. Soc.* **127**, 4580 (2005).
- [6] S.-i. Ohkoshi, H. Tokoro, and K. Hashimoto, *Coord. Chem. Rev.* **249**, 1830 (2005).
- [7] D. Aguilá, Y. Prado, E. S. Koumoussi, C. Mathonière, and R. Clérac, *Chem. Soc. Rev.* **45**, 203 (2016).
- [8] A. Bleuzen, C. Lomenech, V. Escax, F. Villain, F. Varret, C. Cartier dit Moulin, and M. Verdagner, *J. Am. Chem. Soc.* **122**, 6648 (2000).
- [9] M. K. Saha, M. C. Morón, F. Palacio, and I. Bernal, *Inorg. Chem.* **44**, 1354 (2005).
- [10] H. Tokoro, T. Matsuda, T. Nuida, Y. Moritomo, K. Ohoyama, E. Davy, L. Dangui, K. Boukheddaden, and S.-i. Ohkoshi, *Chem. Mater.* **20**, 423 (2008).
- [11] N. Thakur, S. M. Yusuf, P. L. Paulose, and L. Keller, *J. Appl. Phys.* **111**, 063908 (2012).
- [12] V. Escax, A. Bleuzen, C. Cartier dit Moulin, F. Villain, A. Goujon, F. Varret, and M. Verdagner, *J. Am. Chem. Soc.* **123**, 12536 (2001).
- [13] N. Shimamoto, S. Ohkoshi, O. Sato, and K. Hashimoto, *Inorg. Chem.* **41**, 678 (2002).
- [14] C. C. dit Moulin, F. Villain, A. Bleuzen, M.-A. Arrio, P. Sainctavit, C. Lomenech, V. Escax, F. Baudalet, E. Dartyge, J.-J. Gallet, and M. Verdagner, *J. Am. Chem. Soc.* **122**, 6653 (2000).
- [15] S. Bonhommeau, N. Pontius, S. Cobo, L. Salmon, F. M. F. de Groot, G. Molnar, A. Bousseksou, H. A. Kurr, and W. Eberhardt, *Phys. Chem. Chem. Phys.* **10**, 5882 (2008).

- [16] H. Tokoro, S. Miyashita, K. Hashimoto, and S.-i. Ohkoshi, *Phys. Rev. B* **73**, 172415 (2006).
- [17] T. Yokoyama, H. Tokoro, S.-i. Ohkoshi, K. Hashimoto, K. Okamoto, and T. Ohta, *Phys. Rev. B* **66**, 184111 (2002).
- [18] F. M. F. de Groot, J. C. Fuggle, B. T. Thole, and G. A. Sawatzky, *Phys. Rev. B* **42**, 5459 (1990).
- [19] G. van der Laan and I. W. Kirkman, *J. Phys.: Condens. Matter* **4**, 4189 (1992).
- [20] R. K. Hocking, E. C. Wasinger, F. M. F. de Groot, K. O. Hodgson, B. Hedman, and E. I. Solomon, *J. Am. Chem. Soc.* **128**, 10442 (2006).
- [21] D. Asakura, M. Okubo, Y. Mizuno, T. Kudo, H. Zhou, K. Amemiya, F. M. F. de Groot, J.-L. Chen, W.-C. Wang, P.-A. Glans, C. Chang, J. Guo, and I. Honma, *Phys. Rev. B* **84**, 045117 (2011).
- [22] S. Adak, M. Hartl, L. Daemen, E. Fohntung, and H. Nakotte, *J. Electron Spectrosc. Relat. Phenom.* **214**, 8 (2017).
- [23] B. T. Thole, P. Carra, F. Sette, and G. van der Laan, *Phys. Rev. Lett.* **68**, 1943 (1992).
- [24] C. T. Chen, Y. U. Idzerda, H.-J. Lin, N. V. Smith, G. Meigs, E. Chaban, G. H. Ho, E. Pellegrin, and F. Sette, *Phys. Rev. Lett.* **75**, 152 (1995).
- [25] M. Verdagner, T. Mallah, C. H elary, F. L'Hermite, P. Sainctavit, M. A. Arrio, D. Babel, F. Baudelet, E. Dartyge, and A. Fontaie, *Physica B* **208**, 765 (1995).
- [26] E. Dujardin, S. Ferlay, X. Phan, C. Desplanches, C. Cartier dit Moulin, P. Sainctavit, F. Baudelet, E. Dartyge, P. Veillet, and M. Verdagner, *J. Am. Chem. Soc.* **120**, 11347 (1998).
- [27] G. Champion, V. Escax, C. Cartier dit Moulin, A. Bleuzen, F. Villain, F. Baudelet, E. Dartyge, and M. Verdagner, *J. Am. Chem. Soc.* **123**, 12544 (2001).
- [28] J.-D. Cafun, J. Lejeune, J.-Paul Iti e, F. Baudelet, and A. Bleuzen, *J. Phys. Chem. C* **117**, 19645 (2013).
- [29] E. Coronado, M. Carmen Gim enez-L opez, T. Korzeniak, G. Levchenko, F. M. Romero, A. Segura, V. Garc ia-Baonza, J. C. Cezar, F. M. F. de Groot, A. Milner, and M. Paz-Pasternak, *J. Am. Chem. Soc.* **130**, 15519 (2008).
- [30] M.-A. Arrio, J. Long, C. Cartier dit Moulin, A. Bachschmidt, V. Marvaud, A. Rogalev, C. Mathonier e, F. Wilhelm, and P. Sainctavit, *J. Phys. Chem. C* **114**, 593 (2010).
- [31] Y. Prado, M.-A. Arrio, F. Volatron, E. Otero, C. Cartier dit Moulin, P. Sainctavit, L. Catala, and T. Mallah, *Chem. Eur. J.* **19**, 6685 (2013).
- [32] M. L. Baker, Y. Kitagawa, T. Nakamura, K. Tazoe, Y. Narumi, Y. Kotani, F. Iijima, G. N. Newton, M. Okumura, H. Oshio, and H. Nojiri, *Inorg. Chem.* **52**, 13956 (2013).
- [33] S. Kang, H. Zheng, T. Liu, K. Hamachi, S. Kanegawa, K. Sugimoto, Y. Shiota, S. Hayami, M. Mito, T. Nakamura, M. Nakano, M. L. Baker, H. Nojiri, K. Yoshizawa, C. Duan, and O. Sato, *Nat. Commun.* **6**, 5955 (2015).
- [34] S. M. Yusuf, N. Thakur, M. Medarde, and L. Keller, *J. Appl. Phys.* **112**, 093903 (2012).
- [35] J.-Y. Kim, T. Y. Koo, and J.-H. Park, *Phys. Rev. Lett.* **96**, 047205 (2006).
- [36] T. J. Regan, H. Ohldag, C. Stamm, F. Nolting, J. L uning, J. St ohr, and R. L. White, *Phys. Rev. B* **64**, 214422 (2001).
- [37] After the exposure to the soft x-ray synchrotron radiation, the radiation damage was observed in these  $(\text{Rb}_x\text{Ba}_y)\text{MnFe}$  PBA samples. But we have checked that the existence of the  $\text{Fe}^{2+}$  valence states is intrinsic to the bulk of  $(\text{Rb}_x\text{Ba}_y)\text{MnFe}$  PBAs and that the  $\text{Mn}^{2+}$  valence states are very stable in  $(\text{Rb}_x\text{Ba}_y)\text{MnFe}$  PBAs under external perturbations.
- [38] C. Mitra, Z. Hu, P. Raychaudhuri, S. Wirth, S. I. Csiszar, H. H. Hsieh, H.-J. Lin, C. T. Chen, and L. H. Tjeng, *Phys. Rev. B* **67**, 092404 (2003).
- [39] P. Ghigna, A. Campana, A. Lascialfari, A. Caneschi, D. Gatteschi, A. Tagliaferri, and F. Borgatti, *Phys. Rev. B* **64**, 132413 (2001).
- [40] To show the multiplet structures better, rather small values of  $2\gamma = 0.1\text{eV}/0.2\text{eV}$  were used for  $L_3/L_2$  in Figs. 5(a)–5(c). Then, in comparison to the measured spectrum, the  $2\gamma$  value was adjusted to fit the measured peak widths, resulting in  $2\gamma = 0.2\text{eV}/0.4\text{eV}$  for  $L_3/L_2$  [see Figs. 5(d) and 6(d)].
- [41] J.-S. Kang, G. Kim, H. J. Lee, D. H. Kim, H. S. Kim, J. H. Shim, S. Lee, H. G. Lee, J.-Y. Kim, B. H. Kim, and B. I. Min, *Phys. Rev. B* **77**, 035121 (2008).
- [42] D. H. Kim, E. Lee, H. W. Kim, S. Seong, S.-M. Yang, H.-S. Park, J. P. Hong, Y. Kim, J.-Y. Kim, and J.-S. Kang, *J. Magn. Magn. Mater.* **432**, 450 (2017).
- [43] These PBS samples exhibit severe charging problems, and it was difficult to obtain the reliable XAS and XMCD spectra at low temperature ( $T \lesssim 250$  K). We have not succeeded in obtaining the reliable XMCD spectra at  $T \lesssim 250$  K. To overcome a severe charging problem in the XAS/XMCD study of these PBA samples would be very challenging.